Characterizing the Infrared Variability of Protostars Using *WISE* and *NEOWISE*

Daphne Zakarian [1] and John Tobin [2]

[1] *Truman State University*
[2] *National Radio Astronomy Observatory*

ABSTRACT

We investigate the infrared variability of the scattered light nebulae surrounding 63 nearby protostars using archival data from the Wide-field Infrared Survey Explorer (*WISE*) telescope. The 2023 *NEOWISE* data release provides 18 all-sky surveys from 2010 to 2022. We conduct time-series photometry for the nebulae in bands W1 and W2 over this 12 year time period, and we consider targets with a change in flux greater than 15% to show *significant* variability. We detect this level of variability in 59 out of the 63 nebulae in at least one band. This variability is thought to be a consequence of the characteristics of the inner disk structure or overall changes in the source luminosity from variable accretion. In order to further investigate the causes of infrared variability of protostellar nebulae, we propose future work investigating the morphological variability of the sources with higher spatial resolutions. This work will provide further insights into the mechanisms that cause the variability that we have detected among protostellar nebulae.

Keywords: Protostars – Protoplanetary Nebula – Scattered Light Nebulae – Wide-field Infrared Survey Explorer

1. INTRODUCTION

1.1. *Variability of Protostars*

Star formation begins with the collapse of cold molecular clouds. At the center of the collapsing core, a deeply embedded protostar and its associated protoplanetary disk accumulate mass from its dusty, infalling envelope. The dusty envelope and protoplanetary disk are both optically thick at the characteristic wavelengths of the light emitted from the protostar. This results in almost all of the light from the protostar to be absorbed by the surrounding disk and envelope (Hartmann 2009). However, bipolar outflows from the protostar carve out cavities in the envelope as mass is ejected from the protostar. The light from the protostar illuminates the outflow cavities and results in a scattered light nebula that can be observed by infrared observations.

Protostars are exceedingly difficult to observe directly because they are heavily obscured by the envelope and disk. However, spatially resolved scattered light images offer many important insights into the inner disk structure and the variability of the protostar itself. Photometric and morphological variability of scattered light nebulae can be caused by changes in the structure of the outflow cavity itself, but they can also be caused by changes in illumination that result from phenomena such as a disk misalignment, a warped inner disk, other disk asymmetries, unseen companion stars, and intrinsic changes in the protostar's luminosity (Cook et al. 2019).

While we focus on photometric variability for the scope of the project as it stands presently, future work includes investigations of the morphological variability of the sources analyzed in this project. The future work is discussed in more detail in Section 4.

1.2. *Targets*

We investigate the variability of 63 scattered light nebulae with associated protostars. These targets (which are listed in Table 1) were selected because they contain nearby nebulae that are well-resolved by the Spitzer Space Telescope. While variability has not been investigated for many of the targets, the infrared variability for a few of the targets have been previously studied in great detail. A few such examples are listed below.

Connelley et al. (2009) found the infrared nebula associated with the protostar IRAS 18148-0440 to show signs of morphological and photometric variability on the time scale of months. This short timescale for the variability is an indication that the observed variability is likely due to changes in illumination as opposed to changes in the cavity structure. Cook et al. (2019) observe rotating variability in the protostellar nebula L1527 IRS that appears to be consistent with models for a warped inner disk.

2. OBSERVATIONS

2.1. *Wide-field Infrared Survey Explorer*

The Wide-field Infrared Survey Explorer (*WISE*) telescope (Wright et al. 2010) was launched by NASA in 2009 to conduct an all-sky survey in four bands: W1, W2, W3, and W4 with respective wavelengths of 3.4, 4.6, 12, and 22 μm. The *WISE* mission successfully surveyed the entire sky in all four bands before the cryogen was exhausted in 2011, at which point the extended mission known as The *NEOWISE* Post-Cryogenic Mission continued for four months (Mainzer et al. 2011) until the spacecraft was placed into a state of hibernation for 32 months from February 2011 until October 2013. In October 2013, the spacecraft (which is now renamed as the *NEOWISE* telescope) continued with full-sky surveys using bands W1 and W2 for the *NEOWISE* reactivation mission (Mainzer et al. 2014). The reactivation mission is ongoing, and as of June 2023, the *NEOWISE* reactivation mission has resulted in 19 full-sky surveys.

We use observations taken during every phase of the *WISE*/*NEOWISE* telescope's lifetime[1] to investigate the variability of protostars. For simplicity, we will refer to all data collected in any of the *WISE*/*NEOWISE* missions and mission extensions as *WISE* data. Although there are distinctions between the missions, the single-exposure images in bands W1 and W2 are taken and processed identically regardless of which specific mission the observations were taken in. For simplicity we refer to the spacecraft throughout its entire lifetime as the *WISE* spacecraft.

This project utilizes archival data from the WISE mission's all-sky surveys taken between 2010 and 2022. While WISE has taken hundreds of exposures of each target, we divide these exposures into epochs. The epochs correspond to each time WISE passes the target for a survey. During each survey, many exposures of a single target are taken over the span of a few days. All images within those few days share an epoch. Consequently, the epochs for each target are individually assigned.

We use the WISE/NEOWISE Coadder program-line interface[2] to make a coadded image for each epoch. However, the coadder tool's connection time limit was not sufficient for some of the epochs with an excessive number of exposures. The epochs with too many single-exposure images were divided in half in order to meet the connection time limit.

Each coadd consists of a 4'x4' fits file centered around the protostar(s)[3]. After downloading the coadds, we subtracted the background from each image in order to prepare the images for photometric analysis. Because many of the fields contain diffuse, extended sources in the frame, we determine the background signal by scanning the image for the region with the least amount of emission from stellar sources or the target protostellar nebula. For the first epoch of each target, this region with minimum emission (a circular region of 0.5' radius) is used as the background aperture. This aperture position is used to calculate the background for each epoch that the target is observed.

For each epoch coadd, before calculating the median values of the pixels within the background aperture, a mask is applied in order to exclude any sources or bright pixels from the calculation. All pixels with a value greater than 5 times the standard deviation of the entire coadd pixel values are masked. After masking the bright pixels in the image, the median value of the background aperture is calculated and then subtracted uniformly from all pixels in the image.

3. METHODS

We conducted time-series photometry of the targets using the Photutils package from Astropy (Astropy Collaboration et al. 2018) to characterize the photometric variability.

3.1. *Comparison Star Apertures*

Comparison star selection was fully automated in the photometry pipeline using DAOStarFinder in Photutils. DAOStarFinder finds Gaussian-like sources in the image field. We chose the parameters for the star detection in order to detect a few comparison stars even in the least-crowded fields with few available comparison star options. However, in crowded fields, an unnecessarily large number of comparison stars are detected. It is important to note that not all of the detected sources are actually valid comparison stars. Oftentimes, DAOStarFinder places a standard aperture over the target nebulae or another extended object in the field. DAOStarFinder also may detect sources that are saturated. However, all of these issues are addressed later by selective plotting of the higher-quality comparison stars available in the data.

[1] *WISE*/*NEOWISE* missions: the primary WISE mission, the NEOWISE Post-Cryogenic Mission, and the NEOWISE reactivation mission

[2] https://irsa.ipac.caltech.edu/applications/ICORE/docs/ProgramInterface.html

[3] Some fields contain multiple protostars.

We use Photutil's SkyCircularAperture classes[4] to draw identical apertures around each comparison star. For each comparison star, the aperture radius was 8.25"[5], the inner annulus radius was 12", and the outer annulus radius was 18".

3.2. *Target Apertures*

The aperture selection for the targets is considerably less-automated than the comparison star aperture selection because of the diversity of shape, angular size, and background field that the protostars are found in. We used Photutil's SkyEllipticalApertures to draw ellipses around the scattered light nebulae by eye. For each target, the same ellipse is used for every epoch image in both bands. Most fields contain a single protostar and one corresponding elliptical aperture. However, some fields contain multiple target apertures; this was either because we used multiple apertures to separate the bipolar outflows of the nebula, or because there were multiple protostars in the field. In the case where we could easily separate a nebulae by the two outflow cavities, we drew apertures around each cavity independently, and one around the entire system to investigate the total change in flux of both components combined.

3.3. *Photometry*

We use Astropy's TimeSeries class to conduct photometric analysis of the targets and comparison stars. The intensity unit for the pixel values of the WISE coadds is digital numbers (DN). In order to convert the WISE flux measurements into magnitudes, we use the raw flux to magnitude conversions provided by WISE documentation[6].

$$M_{\text{compstar cal Wi}} = M_{0\ \text{Wi}} - 2.5 \times \log_{10}(F_{\text{raw}}) - [\text{AC}] \tag{1}$$

$$M_{\text{target cal Wi}} = M_{0\ \text{Wi}} - 2.5 \times \log_{10}(F_{\text{raw}}) \tag{2}$$

$$F_{\text{v Wi}} = F_{\text{v0 Wi}} \times 10^{(-M_{\text{cal Wi}}/2.5)} \tag{3}$$

$$\delta_{\text{Wi}} = \frac{F_{\text{max Wi}}}{F_{\text{min Wi}}} \tag{4}$$

Equations 1 and 2 are used to convert the raw flux to calibrated magnitude for the comparison stars and target apertures respectively. M_0 is the instrumental zero point (magnitude), F_{raw} is the raw flux from WISE (DN), and $[AC]$ is the aperture correction for standard apertures (magnitude). Note that Equation 2 does not contain aperture corrections because aperture corrections are only applied for standard apertures, not the arbitrarily sized ellipses used for the target photometry. The zero-magnitude flux densities given in Jarrett et al. (2011) are used to calculate the flux density in Equation 3. F_v is the flux density in Jy, and F_{v0} is the zero magnitude flux density in Jy. Equation 4 is used quantify the flux variability of each target, where δ is the multiplicative change in flux for an object. Each calculation is carried out separately for bands W1 and W2, which is denoted by the subscript 'Wi' on relevant measurements and calculations.

3.4. *Visualization of Morphological Variability*

Although the photometry gives important insights into the overall change in flux of the targets, we gain very limited information about the morphological variability of the nebulae. We did apply multiple apertures on a few of the targets with clearly resolved bipolar outflows, but most of the targets only contained one aperture. In order to examine the morphological variability more closely, we create average-subtracted and average-divided images. The average image is created by coadding all of the epoch images into a single average image. For the average-subtracted images, we subtract the average image from each individual epoch image in order to see how the pixel value compares to its average value. This was especially helpful because it can subtract out non-variable background sources. However, as discussed in Section 4, small astrometric offsets between epoch images limit the utility of the average-subtracted images. As such, it is imperative that we address these offsets in the future if we would like to make quantitative measurements using the average-subtracted images.

The average-divided images are created much like the average-subtracted images, except the average is divided from each epoch instead of subtracted (as the name suggests). However the average-divided images did not reflect the variability as clearly as the average-subtracted images. Consequently, we have determined that subtracting the average from each image is the preferred method for future investigations of morphological variability.

[4] SkyCircularAperture is used to ensure consistent placement of the aperture if there are astrometric offsets between epoch images.

[5] the standard aperture radius for WISE bands W1, W2, and W3

[6] https://wise2.ipac.caltech.edu/docs/release/allsky/expsup/sec4_4h.html

4. RESULTS AND DISCUSSION

Qualitatively, the average-subtracted images for each of the 63 nebulae of interest indicate that many of the sources do indeed show infrared variability. We consider nebulae with a maximum flux at least 15% greater than the minimum flux (corresponding to $\delta > 1.15$) to show statistically significant photometric variability over the course of the WISE observations. Out of the 63 protostellar nebulae we studied, 59 are found to show significant variability in at least one band. Our criteria for determining sources with significant variability makes the assumption that a δ greater than 1.15 can be reasonably attributed to the variability of the nebula itself as opposed to random noise in the observations. Furthermore, our decision to use the criteria of 1.15 for δ is justified for WISE observations, because 85% of the comparison stars have δ measured to be less than 1.15. This indicates that δ is typically less than 1.15 for non-variable sources. As such, it is reasonable to assume that the detected variability for larger δ reflects true variability coming from the target. Table 1 displays δ for each target in both bands.

The multiplicative change in flux (δ) quantifies the total variability of each nebulae, but the light curves for each object provide additional insight into how the flux varies throughout the period of observation for each object. The shape of the light curves exhibit a variety of trends. Many show short-term variability but no obvious trend dictating the long-term (10 year) behavior. However, other nebulae clearly display long-term patterns such as steadily increasing, steadily decreasing, concave up, concave down, and clearly periodic trends. Nine of the targets' light curves demonstrating a variety of behaviors can be seen in Figure 1.

5. FUTURE WORK

In the future, we plan to continue this work by adding error bars to the light curves and investigating the morphological variability more closely. The uncertainty measurements provided by WISE will be useful in solidifying our criteria for significant variability detection. In order to investigate the morphological variability of the protostellar nebulae, we first need to address the astrometric offsets between epoch images. The primary motivation for addressing these offsets is the impact that small, pixel-level offsets have on the average-subtracted images. Even small offset between two images results in dramatic effects to the average-subtracted images. This is evident in images with numerous stars in the field of view; the non-variable background stars should be more-or-less completely subtracted out during the average subtraction. However, because of small astrometric offsets, the average image does not directly reflect the correct location for the stars. As a result, the average-subtracted images contain distracting artifacts that occur because the 'average' position of the object doesn't line up with some of the individual epoch images. Improving the average-subtracted images will play a vital role in our future investigation of morphological variability of the nebulae. When aligned properly, average-subtracted images can be used to clearly observe the changes in flux with much-improved spatial resolution.

Investigating the photometric and morphological variability of the scattered-light nebulae surrounding protostars offers important insights into the inner-disk structure of protostellar systems. Although we can not necessarily draw conclusions about the disk structure from these results alone, this project indicates that protostars undoubtedly vary significantly in the infrared over 10 year timescales. Furthermore, these results and the future endeavors of this project may be useful in constraining models of protostellar systems and the mechanisms that contribute to the variable and asymmetric illumination of scattered-light nebulae surrounding protostars.

6. ACKNOWLEDGEMENTS

This work was supported by the NSF Research Experience for Undergraduates (REU) program through the National Radio Astronomy Observatory. The National Radio Astronomy Observatory is a facility of the National Science Foundation operated under cooperative agreement by Associated Universities, Inc.

Table 1. List of positions and multiplicative changes in flux for each object in bands W1 and W2.

Field No.	Target Name	RA	Dec	δ_{W1}	δ_{W2}
1	B335	19:37:01.308	+07:34:8.66	7.354675518	7.653396073
2	BHR7_IRAS08124-3422	08:14:23.326	-34:31:01.24	1.754489156	1.672484057
3	BHR71 IRS1	12:01:36.542	-65:08:54.23	1.493356199	2.638373775
3	BHR71 IRS2	12:01:33.779	-65:08:44.12	2.638373775	1.560036654
4	CB17 IRS	04:04:33.820	+56:56:16.19	1.23610585	1.409326052
5	CB230	21:17:38.600	+68:17:34.15	1.486218782	1.388986459
6	CB244	23:25:46.497	+74:17:38.46	1.824323046	2.858927344
7	CB6	00:49:24.500	+50:44:43.37	1.265176962	1.194776034
8	CB68	16:57:19.540	-16:09:21.45	1.394943798	1.588804527
9	CG30 N (ap0)	08:09:33.148	-36:04:57.82	1.133549936	1.110158714
9	CG30 S (ap1)	08:09:32.319	-36:05:24.32	1.73845706	1.550168343
10	Ced110IRS4	11:06:46.456	-77:22:31.35	1.211533774	1.328582721
11	CepheusE	23:03:12.669	+61:42:24.00	1.774951762	1.581750511
12	DC303.8-14.2	13:07:35.774	-77:00:23.73	1.525717463	2.272070743
13	HH111MMS	05:51:46.171	+02:48:30.01	1.278770609	1.321241343
14	HH270VLA1	05:51:34.646	+02:56:46.75	1.352994303	1.360781969
15	HH46_47	08:25:43.830	-51:00:34.45	1.781858967	2.139670347
16	IRAS03282+3035	03:31:21.131	+30:45:29.38	1.541900224	1.300486704
17	IRAS03292+3039	03:32:18.107	+30:49:45.61	1.280245411	1.302208987
18	IRAS04166+2706	04:19:42.737	+27:13:40.82	1.502256203	1.565027304
19	IRAS04169+2702	04:19:58.463	+27:09:57.10	1.755652333	1.585204168
20	IRAS04302+2247	04:33:16.474	+22:53:20.48	1.980524147	2.007749112
21	IRAS04325+2402 AB	04:35:35.410	+24:08:19.98	1.174432933	1.190170524
21	IRAS04325+2402 C	04:35:36.348	+24:08:56.95	1.18024608	1.193247902
22	IRAS05295+1247	05:32:19.798	+12:49:56.98	2.458251851	1.943681222
23	IRAS05329-0505	05:35:26.638	-05:03:54.99	1.166762983	1.256802425
23	TKK 870	05:35:28.184	-05:03:41.34	2.157446451	1.995355789
24	IRAS09449-5052	09:46:45.823	-51:06:06.15	1.201818001	1.211645326
25	IRAS11072-7727	11:08:38.927	-77:43:51.35	1.175993297	1.227333146
26	IRAS15398-3359	15:43:02.067	-34:09:09.92	2.834207889	1.481584721
27	IRAS16253-2429	16:28:23.199	-24:36:05.71	6.075132099	2.07466389
27	MMS126	16:28:21.685	-24:36:22.60	33.49466409	2.089746257
27	MMS060	16:28:20.069	-24:36:51.29	2.256564185	1.695562374
28	IRAS02086	02:13:37.572	+76:15:01.58	1.420123773	1.348915707
29	L1152	20:35:46.249	+67:53:01.68	1.134286827	1.254783806
30	L1157	20:39:06.317	+68:02:12.39	1.393973363	1.229393536
31	L1165	22:06:50.302	+59:02:44.91	1.170508553	1.18864763
32	L1251A	22:38:52.932	+75:11:23.27	1.346755619	1.310047217
32	2MASS J22391329+7512161	22:39:13.314	+75:12:15.86	4.685642214	3.933579935
32	CXOU J223846.9+751133	22:38:46.898	+75:11:33.69	1.869647224	2.074898413
33	L1251B	22:31:05.598	+75:13:37.46	1.375483224	1.215054335
34	L1251C	22:30:31.571	+75:14:00.74	1.11930983	1.122361417
35	L1448IRS2	03:25:22.304	+30:45:13.70	1.370303388	1.330071344
36	IRAS 03225+3034 NE	03:25:36.573	+30:45:27.77	1.254443577	2.578178999
36	JCMTSE J032536.1+304514 NW	03:25:35.818	+30:45:16.45	1.369825018	2.338883596
36	IRAS F03226+3033 SE	03:25:39.129	+30:43:58.91	4.485467713	3.459936911

Continued on the next page

Table 1 – Continued from previous page

Field No.	**Target Name**	**RA**	**Dec**	δ_{W1}	δ_{W2}
36	L1448mms SW	03:25:38.680	+30:44:07.89	4.715037083	2.464724563
37	L1489IRS	04:04:43.068	+26:18:56.32	2.271573096	1.849326776
38	L1521F	04:28:38.685	+26:51:34.94	1.547414436	1.602283842
39	L1527_IRAS04368+2557	04:39:53.692	26:03:08.28	1.580692923	1.395066853
40	L1551IRS5	04:31:34.088	+18:08:04.90	1.197913495	1.512686669
41	L1551NE	04:31:42.067	+18:08:13.95	1.089894682	1.132032193
42	L1616MMS1A	05:06:44.627	-03:21:37.41	1.107666462	1.408335226
43	L1634	05:19:48.190	-05:52:04.49	1.592205636	1.437406553
43	L1634 W	05:19:51.816	-05:52:09.27	3.064929515	3.170116534
44	L483 (IRAS 18148-0440)	18:17:30.077	-04:39:38.31	3.395122308	2.588355154
45	L723_IRAS19156+1906	19:17:53.757	+19:12:18.75	1.322659305	1.26438392
46	L778	19:26:32.079	+23:58:44.74	2.411388703	2.364634343
47	RCrAIRAS32	19:02:58.686	-37:07:35.11	1.111131225	1.129013388
48	Ser-emb-21	18:29:51.211	+01:16:39.61	4.65571056	5.380506116
48	Ser-emb-06	18:29:49.552	+01:15:29.91	6.704800707	5.303270702
49	Ser-emb-01	18:29:08.963	+00:31:22.90	1.203737368	1.349029305
49	Ser-emb-17 & Ser-em-18	18:29:06.523	+00:30:36.46	8.333222254	6.062416585

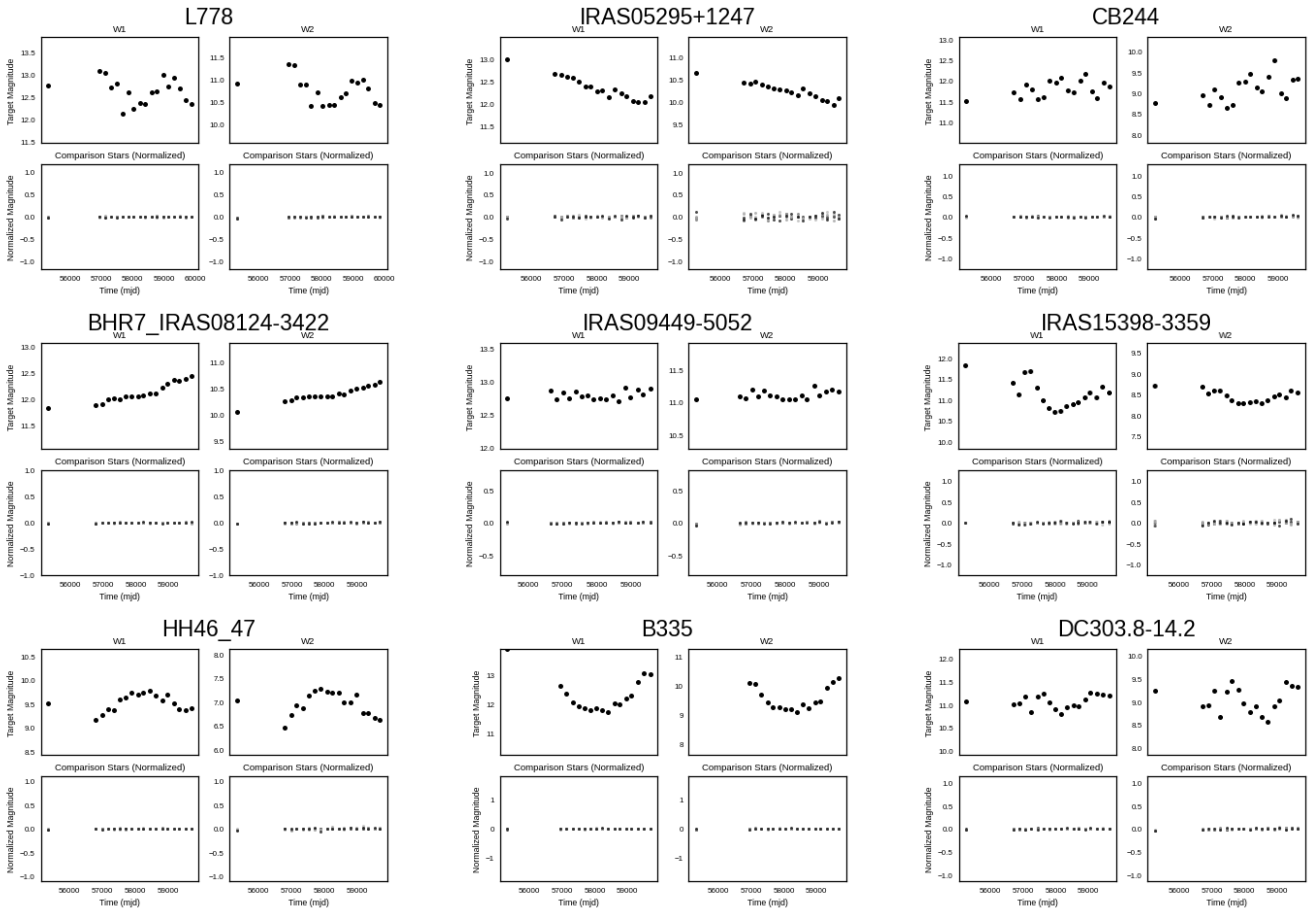

Figure 1. Light curves for a protostar in NEOWISE bands W1 and W2 (top panels), with comparison stars for reference (lower panels). The top panels show variability.

REFERENCES

Astropy Collaboration, Price-Whelan, A. M., Sipőcz, B. M., et al. 2018, AJ, 156, 123, doi: 10.3847/1538-3881/aabc4f

Connelley, M. S., Hodapp, K. W., & Fuller, G. A. 2009, The Astronomical Journal, 137, 3494, doi: 10.1088/0004-6256/137/3/3494

Cook, B. T., Tobin, J. J., Skrutskie, M. F., & Nelson, M. J. 2019, Astronomy and Astrophysics, 626, A51, doi: 10.1051/0004-6361/201935419

Hartmann, L. 2009, Accretion Processes in Star Formation, 2nd edn. (Cambridge University Press)

Jarrett, T. H., Cohen, M., Masci, F., et al. 2011, The Astrophysical Journal, 735, 112, doi: 10.1088/0004-637X/735/2/112

Mainzer, A., Bauer, J., Grav, T., et al. 2011, The Astrophysical Journal, 731, 53, doi: 10.1088/0004-637X/731/1/53

Mainzer, A., Bauer, J., Cutri, R. M., et al. 2014, The Astrophysical Journal, 792, 30, doi: 10.1088/0004-637X/792/1/30

Wright, E. L., Eisenhardt, P. R. M., Mainzer, A. K., et al. 2010, The Astronomical Journal, 140, 1868, doi: 10.1088/0004-6256/140/6/1868